ACS NANO

Operando Bragg Coherent Diffraction Imaging of $LiNi_{0.8}Mn_{0.1}Co_{0.1}O_2$ Primary Particles within Commercially Printed NMC811 Electrode Sheets

Ana Katrina C. Estandarte, Jiecheng Diao, Alice V. Llewellyn, Anmol Jnawali, Thomas M. M. Heenan, Sohrab R. Daemi, Josh J. Bailey, Silvia Cipiccia, Darren Batey, Xiaowen Shi, Christoph Rau, Dan J. L. Brett, Rhodri Jervis, Ian K. Robinson, and Paul R. Shearing*

Cite This: https://dx.doi.org/10.1021/acsnano.0c08575 Read Online

ACCESS | Metrics & More | Article Recommendations | Supporting Information

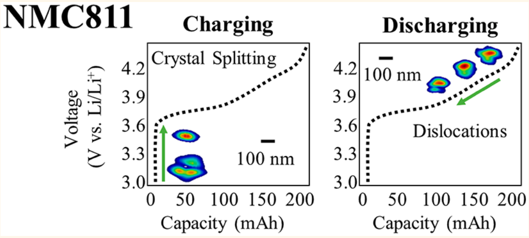

ABSTRACT: **Due to complex degradation mechanisms, disparities between the theoretical and practical capacities of lithium-ion battery cathode materials persist. Specifically, Ni-rich chemistries such as $LiNi_{0.8}Mn_{0.1}Co_{0.1}O_2$ (or NMC811) are one of the most promising choices for automotive applications; however, they continue to suffer severe degradation during operation that is poorly understood, thus challenging to mitigate. Here we use *operando* Bragg coherent diffraction imaging for 4D analysis of these mechanisms by inspecting the individual crystals within primary particles at various states of charge (SoC). Although some crystals were relatively homogeneous, we consistently observed non-uniform distributions of inter- and intracrystal strain at all measured SoC. Pristine structures may already possess heterogeneities capable of triggering crystal splitting and subsequently particle cracking. During low-voltage charging (2.7−3.5 V), crystal splitting may still occur even during minimal bulk deintercalation activity; and during discharging, rotational effects within parallel domains appear to be the precursor for the nucleation of screw dislocations at the crystal core. Ultimately, this discovery of the central role of crystal grain splitting in the charge/discharge dynamics may have ramifications across length scales that affect macroscopic performance loss during real-world battery operation.**

KEYWORDS: *Li ion, X-ray, synchrotron, CDI, NMC811, operando, electric vehicle*

One of the most promising families of cathode materials for automotive batteries are lithiated transition metal layered oxides of the form $Li(Ni_xMn_yCo_{1-x-y})O_2$ (or NMC). They have favorable capacities (>200 mAh g^{-1})[1,2] compared with other intercalation compounds[3] and, if Ni-rich, also offer enhanced rate capabilities and a reduced Co fraction, which has positive environmental, ethical, and cost implications.[1] However, it has been well documented that decreased structural and thermal stability accompanies this increased Ni content.[4,5] NMC811, for example, has a theoretical capacity of 278 mAh g^{-1}; however, the practical capacity is often significantly lower (~200 mAh g^{-1} at 4.3 V *vs* Li/Li^+).[6] Higher practical capacities may be achieved by increasing the upper cutoff voltage during operation, *e.g.* from 4.3 to 4.5 V *vs* Li/Li^+, but at a cost of accelerated degradation and instability resulting in capacity fade, poor cycle life, and safety issues.[7−9]

Battery electrodes are complex, composite materials with morphological characteristics spanning the nanometer to micrometer length scale. Commercial NMC811 materials consist of printed electrode sheets constituting many millions of secondary particles, each *ca.* 3−30 μm in diameter. The secondary particles are constructed as agglomerates of much smaller primary particles, on the scale of *ca.* 100 nm to 1 μm, while the primary particles are thought to contain very few domains or even be single crystals.[10] The recent development and proliferation of X-ray tomography tools has provided

Received: October 14, 2020
Accepted: December 8, 2020

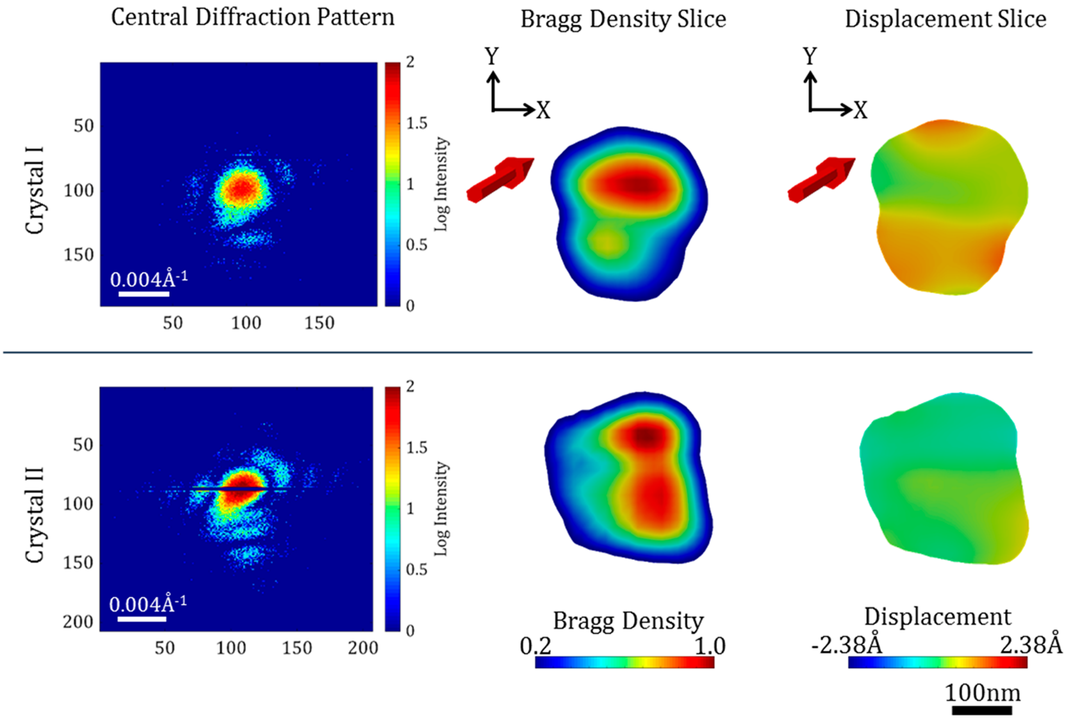

Figure 1. BCDI characterization of *ex situ* pristine NMC811 for crystals I and II, displaying the central diffraction pattern, Bragg density, and displacement slices taken near the center of the crystals.

insight into the real microstructure of battery materials, revealing their hierarchical structure in 3D;[11,12] these can be extended into the fourth dimension to evaluate the changes in microstructure with time and in response to a range of external stimuli.[13] At each discrete length scale there is a growing body of data, but the resolution limits of conventional (full-field) X-ray imaging techniques have limited our understanding at the nanoscale. Meanwhile, transmission electron microscopy (TEM) studies provide near atomic resolution but must employ *in situ* cells which depart from real cell architectures and operating conditions, as well as the electrolytes and materials being susceptible to beam damage during imaging.[14] Moreover, the acquisition and reconstruction of 3D data can prove difficult in TEM, especially for *operando* battery studies.

Bragg coherent diffraction imaging (BCDI) is an X-ray imaging technique which allows the 3D strain within individual crystals to be mapped at the atomic scale.[15,16] The use of hard X-rays allows sufficient penetration inside a working battery environment to examine the components under *operando* conditions. The 3D structure of the object in real space is reconstructed from the measured coherent diffraction pattern using iterative phase retrieval algorithms.[17,18] Coherent X-ray beams are required to produce the interference fringes from the crystal grains, which are available at state-of-the-art synchrotron X-ray sources such as the Diamond Light Source used in this work. The reconstructed object consists of the Bragg electron density, which shows the crystal morphology, and the phase, which corresponds to the projection of the lattice distortions within the crystal onto the direction of the measured Bragg peak.[15] The Bragg density is the amplitude of the image measured at a particular Bragg peak. Its value informs us how strongly that part of the sample contributes to the Bragg peak. The value can drop if the sample region becomes disordered or if it changes orientation to no-longer satisfy the Bragg condition. BCDI has a spatial resolution of 10–20 nm; however, the strain sensitivity is at the picometer level, in the sense that a phase shift of 2π corresponds to a displacement equivalent to one lattice spacing of the $(h\ k\ l)$ plane for a chosen Bragg peak.

Previous BCDI studies on battery materials by Ulvestad *et al.* showed the formation of dislocations in individual $LiNi_{0.5}Mn_{1.5}O_4$ (LNMO)[19] and Li-rich layered oxide (LRLO), $Li_{1.2}Ni_{0.13}Mn_{0.53}Co_{0.13}O_2$,[20] nanoparticles under *operando* conditions using a kapton-windowed coin cell. These dislocations facilitated phase transformation in the LNMO and contributed to voltage fade in the LRLO material during charging. However, housing air-sensitive materials within assemblies that employ windows (rather than being entirely sealed like a commercial cylindrical or pouch cell) can be highly challenging;[21] for instance, NMC811 is particularly susceptible to reactions with moisture and CO_2 in the air, and thus the authors concluded that the kapton-windowed coin cells employed in pervious *operando* BCDI experiments would not be suitable for studying NMC chemistries with high Ni content without inducing significant degradation in the materials.[22]

Although high-resolution secondary particle studies (on the scale of 5–30 μm) have produced significant advancements in our understanding of the complex stress distributions responsible for secondary particle deformation and damage,[23−27] investigations into the structures of NMC beyond the scale of secondary particles (*i.e.*, primary particles on the sub-micrometer scale) are very few and often require *ex situ* 2D methods.[28] There thus remains a fundamental lack of understanding of how the morphology and crystallographic strain of the primary particles, and individual crystals, within NMC, change during cycling and how this affects the electrochemical performance of the material. Improved insight into the morphological changes at the primary particle level within commercial NMC materials is vital.

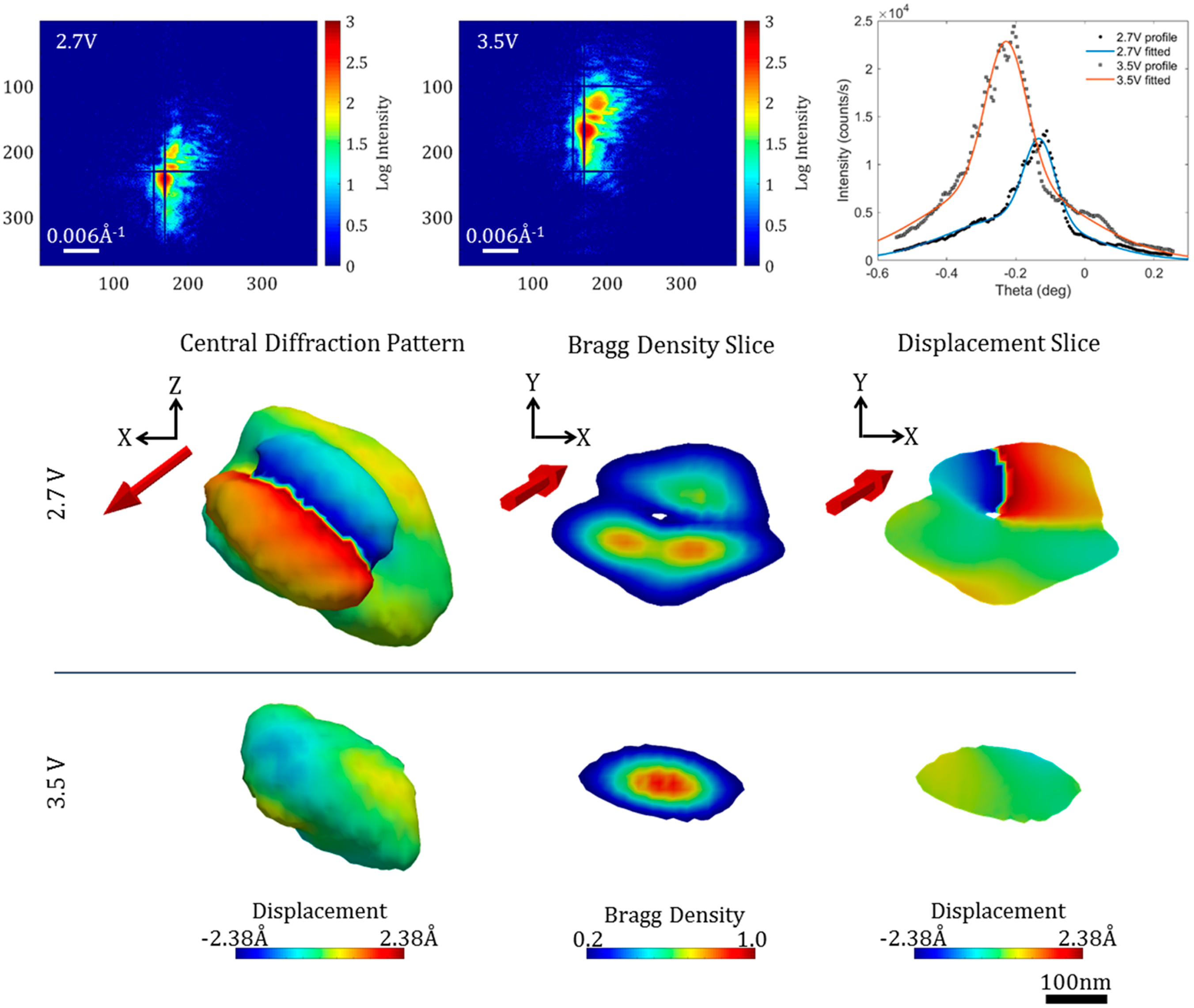

Figure 2. BCDI characterization of NMC811 for crystal III during charging, displaying the central diffraction pattern for 2.7 and 3.5 V, with accompanying plots for the experimental (dots) and Gaussian-fitted (solid lines) data. The reconstructed images of crystal III are also presented with the Bragg density and displacement slices taken near the center of the crystal.

This work, recording the 3D structural changes in individual crystals by BCDI during *operando* charging and discharging cycles extends our knowledge of NMC811 degradation at resolutions beyond secondary particles by mapping the structural dynamics of individual crystals. The mechanisms that result in crystal domain distortion, splitting, and shrinkage may have performance ramifications up to the cell level and thus greatly improve our understanding of these complex materials. Moreover, the experimental procedure outlined here for conducting 4D BCDI investigations into electrochemically operational commercial cathodes is one that is not limited to NMC but may be extended to explore other promising next-generation materials.

RESULTS

Pristine NMC811 Crystals. To develop a comprehensive understanding of the particle dynamics within operating NMC811, several crystals have been examined in this work and they have been numbered accordingly, *e.g.*, crystal I, II, and III, *etc.* Figure 1 displays the central diffraction patterns of crystal I and II from the pristine NMC811 material that was examined *ex situ* (further images of NMC811 powder, the cell housing, and pristine reconstructions can be found in the Supporting Information: Figures S1−S3). The relatively high degree of symmetry observed within these patterns signifies minimal strain (where displacement is near 0 Å or very small) within the crystals compared to the crystals reconstructed during the *operando* experiments (where displacement is notably greater than 0 Å, *e.g.*, over ±2.3 Å); this will be discussed within the subsequent sections.

Figure 1 also shows the reconstructed Bragg density and displacement slices taken near the center of the crystals imaged with the (003) reflection. Although the diffraction patterns display high symmetry, both of the crystals show a single center split into two lobes in the Bragg density slice. Positive values in the displacement slice represent displacements from the ideal crystal lattice along the direction of the **Q**-vector, (003) in this case; conversely, negative values are along the direction opposite to that of the **Q**-vector. These reconstructions suggest non-uniform intercrystal strain distributions. However, even at this early stage of cell life, there is also evidence of heterogeneous intracrystal strain distribution. The crystals have both positive and negative displaced regions in the core and on the surface, showing that the crystals are under shear strain, which could possibly lead to the splitting behavior. It is well-reported that the lithiation and delithiation processes cause various, and often nonlinear, expansion and contraction of the lattice constants,[29] so the strain on the two crystals may be due to inhomogeneous de/lithiation of the crystals during the diagnostic/formation cycle.

NMC811 Crystals during Charging. It is well-documented that, at low voltages, where the layered NMC structure is highly lithiated, minimal charge transfer occurs between the electrodes because Li^+ mobility is low; *i.e.*, negligible amounts of Li^+ ions leave the NMC structure and travel to the counter electrode (Li metal in this case), thus producing a differential charge profile with a gradient close to zero.[30−32] Consequently, up to a cell potential of *ca.* 3.6 V (*vs* Li/Li^+), the average primary particle should undergo minimal change apart from an increase in the local electrochemical potential. However, this assumes both the inter- and intraparticle state of charge are homogeneous.

We measured the diffraction from crystal III during a charging step in a horizontal diffraction geometry (see Methods for setup and Figure S4 for the electrochemistry). If its state of charge were higher than the bulk material, *i.e.*, it had begun delithiating, the Bragg angle should shift between the 2.7 and 3.5 V acquisitions. Figure 2 displays the central diffraction patterns of crystal III at 2.7 and 3.5 V, respectively. During charging, the center of mass (COM) of the diffraction pattern moved upward along the powder ring by 70 pixels, as listed in Table S1 (also see Table S2 and the accompanying explanation within the Supporting Information). This movement along the powder ring can be attributed to the rotation of the crystal around the Bragg condition by 0.0745°. However, there was no apparent shift in the Bragg angle of the diffraction pattern, signifying that the average d_{003} spacing of crystal III did not change during charging to 3.5 V, as might have been expected. Figure 2 also shows the intensity profiles and their Gaussian fit of crystal III upon charging, where the intensity increased by a factor of 2. Notably, there is a 0.0963° peak shift in the negative 2θ direction, as listed in Table 1, and a corresponding small change in its position on the detector. This can be attributed to compound angular movements within the secondary particle agglomerate.

Although the Bragg angle of the reconstructed crystal does not change between 2.7 and 3.5 V, the crystal volume reduces substantially. Figure 2 also displays the BCDI reconstructed images of crystal III at 2.7 and 3.5 V. The Bragg density slice at 2.7 V shows that the crystal is split into two centers or domains, with a low-density gap in between, and the bottom domain starting to form another center. The characteristic phase pattern that can be observed from the contour view and displacement slice at 2.7 V is due to the presence of a mixture of screw and edge dislocations on the top domain of crystal III.[33] Locally around the dislocation (within 100 nm) a gradient in the displacement slice can be observed with peaks of *ca.* ±2.38 Å. As mentioned, the crystal morphology changed significantly after charging to 3.5 V; the reconstructed images show that the crystal is smaller, with the Bragg density slice showing one center. There are two possible reasons for the change in crystal size: the part of the crystal (the domain) that is no longer visible either underwent excessive delithiation (relative to the bulk) or reoriented and no longer satisfies the Bragg condition for this setup. An inhomogeneous distribution of Li^+ within the layered NMC structure could cause a significant shift in the lattice parameter, thus inducing a change in the reflected Bragg angle (see Supporting Information for a more detailed reasoning). This would, however, have required a substantial disparity between the crystal's local state-of-charge (SoC) and the SoC of the bulk material. The other possibility is that a reorientation (without resizing) of the part of the crystal that broke away now reflects at a different point on the Debye−Scherrer ring, thus a change in the reflected azimuthal position.

Table 1. Summary of the Five Crystals Examined in This Work, for the Three Types of Studies: Pristine, Charging, and Discharging[a]

investigation	crystal	acquisition type	state of charge during imaging
1. pristine	I	*ex situ* disconnected from the potentiostat	discharged to 3.0 V at C/20
	II		disassembled and imaged
2. charging	III	*operando* during an electrochemical potential hold after *in situ* cycling	held at 2.7 V during imaging; charged at C/2
			held at 3.5 V during imaging
3. discharging	IV		held at 4.1 V during imaging; discharged at C/2
			held at 4.0 V during imaging; discharged at C/2
	V		held at 3.9 V during imaging

[a] An indication of the state of charge of the electrode at the time of imaging is given by the accompanying cell potential.

In conclusion, crystal III was structurally dynamic during a cell potential window (2.7−3.5 V) that is widely reported to contain minimal charge transfer.[2,30,31] Furthermore, there was no observable shift in the Bragg angle at 3.7 V, confirming that the crystal volume that remained after charging had undergone minimal delithiation. There was, however, a region of the crystal that was lost from the observable Bragg orientation, and therefore not reconstructed, that is thought to have split from the volume observed at 2.7 V due to a dislocation. Hence, we have observed crystal splitting during a part of the charge profile associated with negligible deintercalation of Li^+ from the layered NMC structure at the bulk scale.

NMC811 Crystals during Discharging. Figure 3 displays the central diffraction patterns from crystal IV during discharging from 4.1 V, to 4.0 V, and finally to 3.9 V (see Figure S4 for electrochemistry). Crystal V, which was situated in the near vicinity of crystal IV, was also examined and can be found in the Supporting Information. The intensity of the diffraction patterns decreased as the crystals were discharged, *i.e.*, as the layered NMC structure was lithiated. Reductions in the (003) reflection can be an indication of cation mixing when compared as a ratio to other peaks such as the (104) peak; however, they may also simply signify a reduction in the degree of ordering or increased displacement within the crystal, *e.g.*, intraparticle heterogeneities. Due to limitations of BCDI at I-13, only the (003) reflection could be examined; consequently, assessing the peak ratio was impossible. Nonethe-

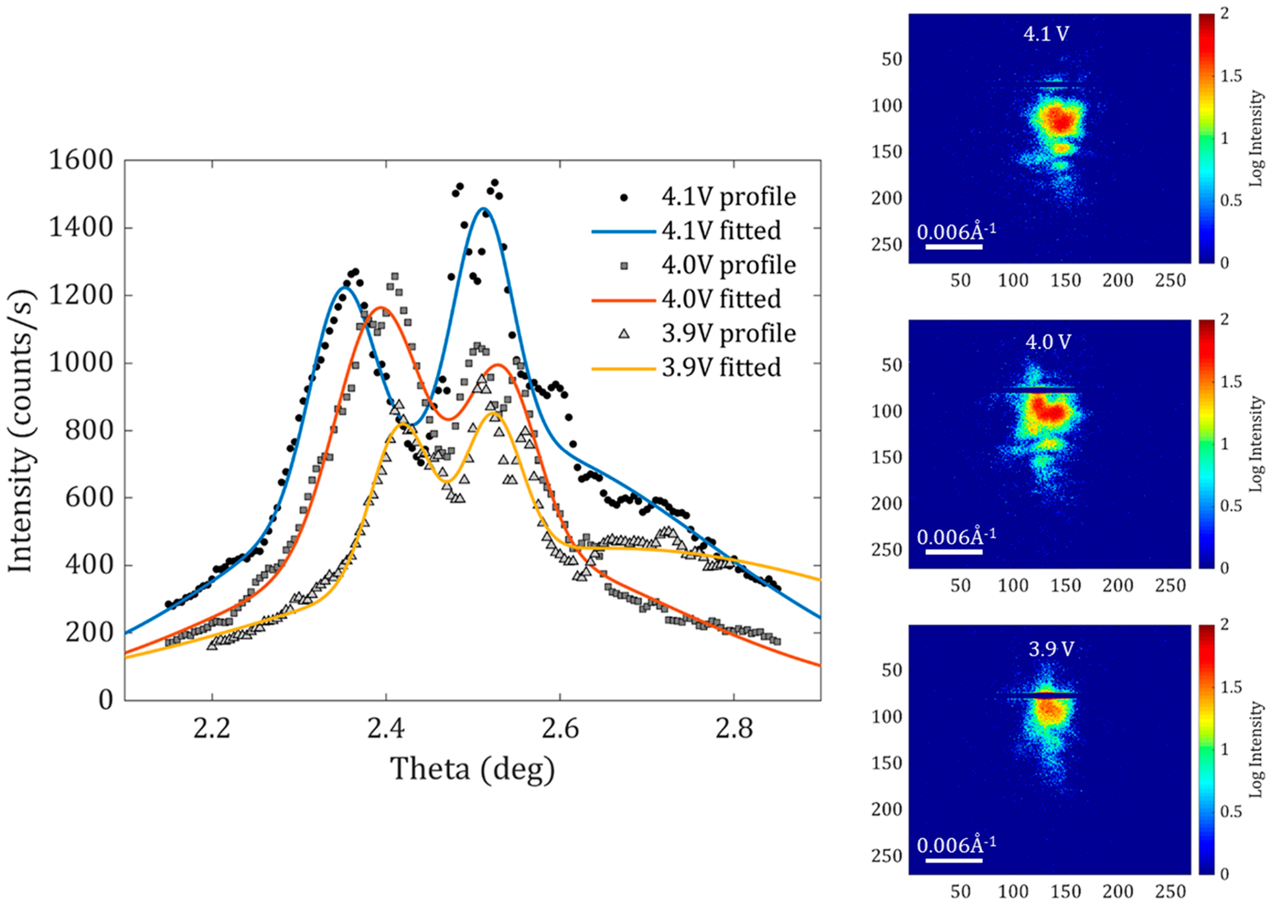

Figure 3. BCDI characterization of NMC811 for crystal IV during discharging, displaying the central diffraction patterns for 4.1, 4.0, and 3.9 V, with accompanying plots for the experimental (dots) and Gaussian-fitted (solid lines) data.

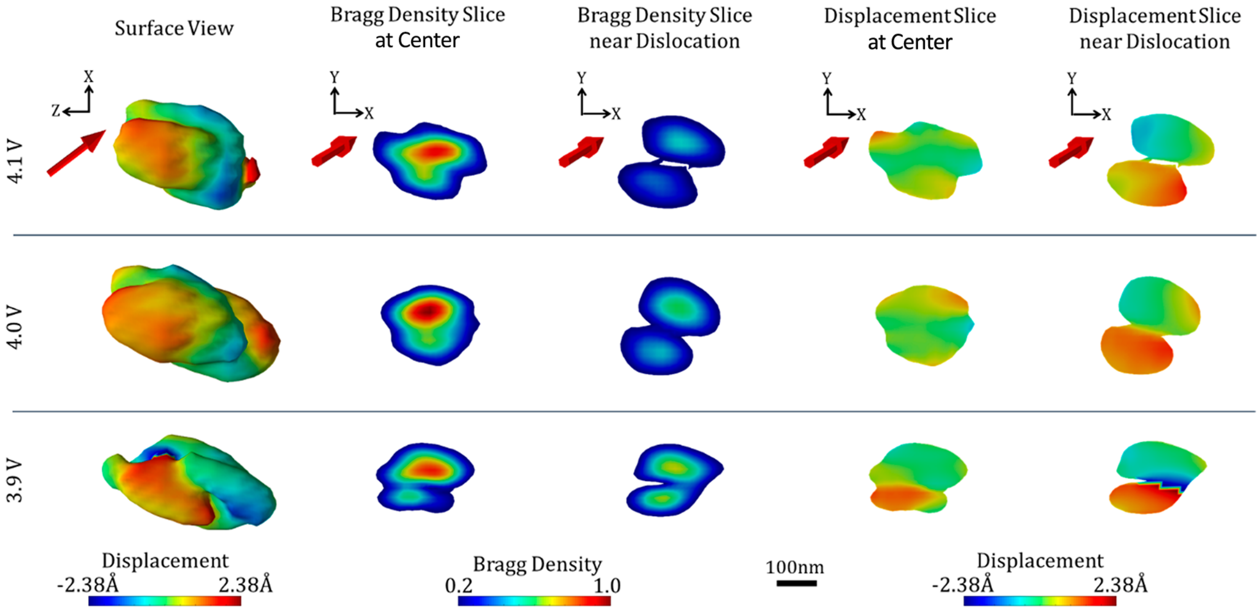

Figure 4. BCDI characterization of NMC811 for crystal IV during discharging, displaying the reconstructed images of crystal IV, presented with the Bragg density and displacement slices taken near the center of the crystal and near a dislocation.

less, as with the previous crystals I–III, the Bragg density and displacement could be mapped.

As was seen in crystal III central diffraction patterns, the COM of the crystal IV diffraction patterns also moved up around the powder ring during discharge, showing the rotation of the crystals around the Bragg condition. However, unlike crystal III, the whole intensity profile of crystal IV shifted to a more positive 2θ angle by around 9–10 pixels, indicating a

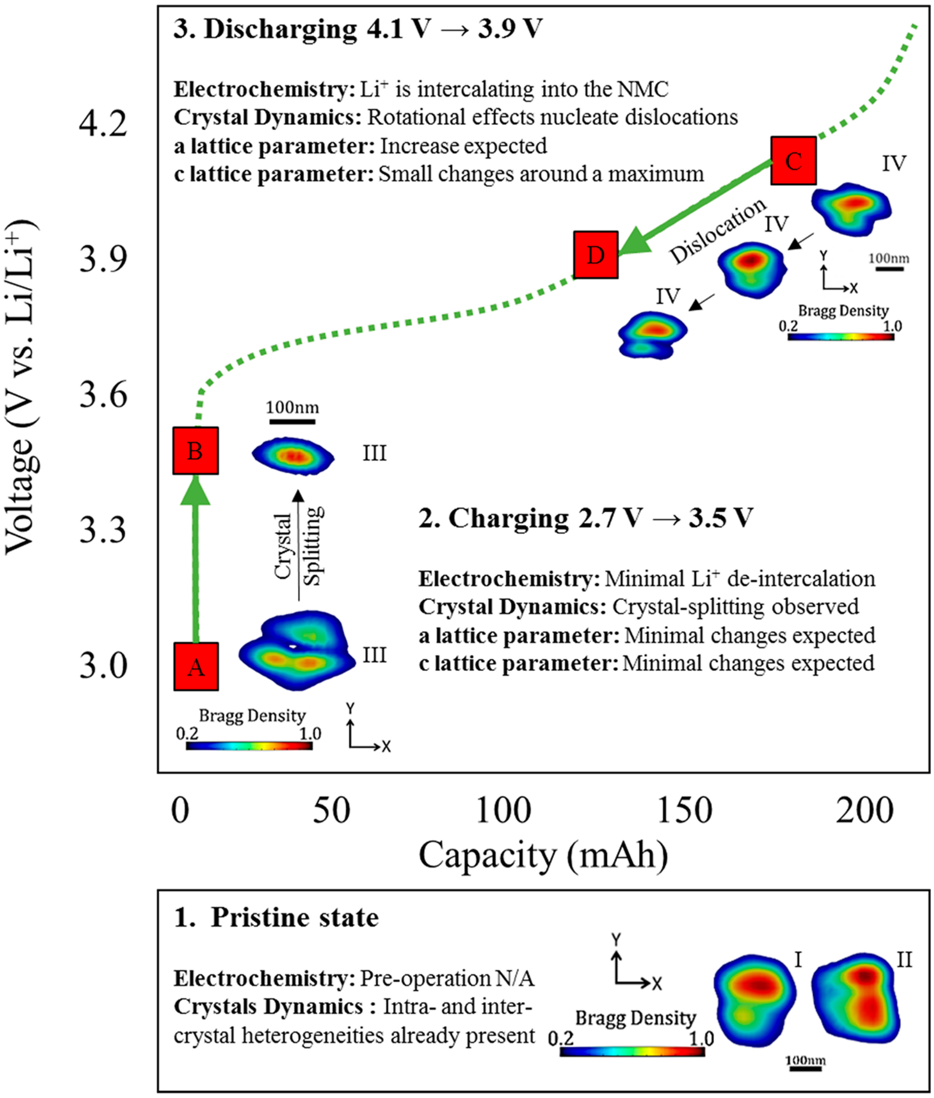

3. Discharging 4.1 V → 3.9 V

Electrochemistry: Li^+ is intercalating into the NMC
Crystal Dynamics: Rotational effects nucleate dislocations
a lattice parameter: Increase expected
c lattice parameter: Small changes around a maximum

2. Charging 2.7 V → 3.5 V

Electrochemistry: Minimal Li^+ de-intercalation
Crystal Dynamics: Crystal-splitting observed
a lattice parameter: Minimal changes expected
c lattice parameter: Minimal changes expected

1. Pristine state

Electrochemistry: Pre-operation N/A
Crystals Dynamics : Intra- and inter-crystal heterogeneities already present

Figure 5. Example of a generic NMC811 charge/discharge curve with accompanying annotation of the three mechanisms observed here: (1) underlying heterogeneities in pristine material, (2) crystal splitting even when minimal bulk deintercalation is present, and (3) dislocation formation during the re-lithiation of the layered NMC811 structure.

very small shift in the d_{003} spacing. Therefore, unlike crystal III, which is thought not to have undergone deintercalation during the charging from 2.7 to 3.5 V, the data suggest that crystal IV *has* undergone Li^+ intercalation during discharge from 4.1 to 3.9 V. This is corroborated by the well-reported differential capacity profiles for bulk NMC811 during charge/discharge cycling.[30−32] Next, we explore the structural dynamics during this discharge process that may be responsible for the loss in Bragg reflection intensity.

Figure 4 shows the reconstructed images of crystal IV. The Bragg density slice shows a clear boundary dividing the crystal, suggesting it is split into two parallel domains. During discharge, there is one domain that becomes split in two near the center of the crystal, while the two domains at the left edge of the crystal become joined. Further values on crystal IV can be found in the Supporting Information (Table S3). The Bragg density slice near the center of the crystal indicates a domain on the order of 200−300 nm in diameter, whereas the Bragg density slice taken from near the dislocation displays two domains each *ca.* 150 nm in diameter. The displacement field shows positive and negative displaced regions at 4.1 V. When the crystal was discharged from 4.1 to 4.0 V, the positive displacement in the crystal increased while the negative counterpart decreased. This displacement pattern and the Bragg density slices signify that the two domains of the crystal are rotating slightly with respect to each other due to the discharging action; *i.e.*, the Li^+ intercalation mechanisms are triggering structural dynamics in the crystal domains. When further discharged to 3.9 V, a screw dislocation is formed in the crystal core between the two domains. The rotation effect appears to be a precursor of the nucleation of a dislocation, akin to the classical shear mechanism of dislocation formation.[34]

Conversely, there were no significant changes observed for crystal V upon discharge (Figure S5 and S6 and Table S4 in the Supporting Information), which further corroborates what was seen within the pristine and charging crystals: both intra- and interparticle heterogeneities exist in this commercial NMC811 electrode; *i.e.*, there are differences in the crystal Bragg densities and displacements both across individual particles and between neighboring particles. It may be that

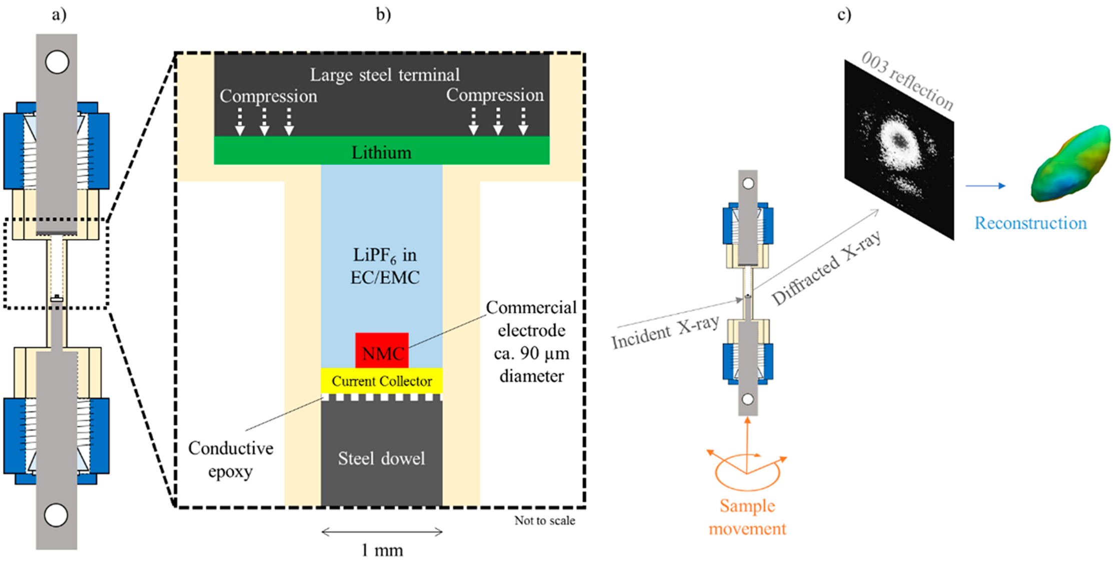

Figure 6. Experimental setup for conducting 4D BCDI investigations into Li-ion battery cathode materials: (a) bespoke cell with PEEK housing, steel terminals, and PFA Swagelok seals, (b) magnified schematic of the NMC electrode and lithium metal which are parted without the use of a separator but connected electrochemically *via* a $LiPF_6$ electrolyte, and (c) the Diamond Light Source I13-1 beamline acquisition setup with the incident and diffracted X-ray beam, (003) reflection observed on the detector, and the reconstruction of an NMC crystal.

crystal V appeared inactive because it had become electrically disconnected from the rest of the secondary particle.

Degradation of NMC811 Crystals during Operation. Figure 5 provides a visual summary of the insight gained in this work and attempts to map each mechanism's corresponding location on a generic charge/discharge curve. First, the pristine material that had only undergone diagnostic/formation cycles exhibited high symmetry, compared with the majority of the crystals examined during electrochemical operation. However, their behaviors were found to be inhomogeneous; pristine crystals I and II already exhibited signs of intra- and intercrystal heterogeneities even before operational cycling. It is thought that such pre-existing heterogeneities could seed further dislocations and even splitting of the crystals upon further cycling. Second, crystal III was seen to split during charging from 2.7 to 3.5 V, a region of the charging curve where it is well-reported that minimal charge transfer occurs at the bulk scale; *i.e.*, the differential capacity curve in this region has a gradient close to zero, and thus the crystallographic changes due to electrochemical activity are negligible.[30−32] We infer that this crystal either split due to a substantial disparity between the local and bulk SoC or reoriented and broke away from the initial crystal structure without delithiating; either way, this provides evidence that crystal-scale dynamics may still be present even before significant bulk charge transfer has begun. Third, during discharge, rotational effects located at the crystal core may nucleate dislocations that are exacerbated by the changes in the local lattice parameter due to the intercalation of Li^+ into the layered NMC structure, ultimately triggering strain and crystal splitting (Figure S7). The rotational nature of these dislocations may be due to the various orientations of the crystals within the secondary particle agglomerate. Neighboring but misaligned crystals are inherent in polycrystalline materials, and the boundaries between such primary particles present opportunities for inter- and intracrystal splitting; the heterogeneous lithiation of the electrode material could exacerbate these misalignments, causing crystals to split or neighboring crystals to separate in order to reduce the local stress of the system, ultimately degrading the material and disrupting Li-conduction pathways.

CONCLUSION

This work employs time-resolved 4D BCDI to characterize the crystal structures of individual primary particles within NMC811 battery cathode material. Through electrochemical cycling that is representative of operation within commercial devices, we have presented information gathered from a pristine electrode and material undergoing charging and discharging processes. The results reported here provide evidence that intra- and intercrystal heterogeneities can exist even before operational cycling. Moreover, during charging crystal-scale dynamics may be present before significant bulk charge transfer has begun; and during discharge, strain and crystal splitting can occur even during the first operational cycle. The *operando* BCDI methodology and insight presented here have extended our understanding of the crystal-scale dynamics within the next-generation NMC811 battery cathode material. Such mechanisms are thought to be responsible for particle cracking and oxygen release, leading to the loss of performance at the cell level. Gaining an improved understanding of the mechanisms in terms of how they initiate and propagate will ultimately aid in the intelligent development of future battery electrode materials.

METHODS

Cell Housing. Building upon previous work where we developed bespoke cell geometries for specific X-ray characterization methods,[21] we developed a cell holder optimized for Bragg geometry experiments. Unlike other experiments reported within the literature which have employed coin cells or windows, the moisture sensitivity of this material necessitated the development of an airtight housing. Moreover, the development of a versatile housing that may be used for other methods has the added benefit of the potential for future correlative studies. For example, this cell design may be used for traditional full-field imaging or other advanced characterization methods. Furthermore, the amount of material within the diffracted beam path should be minimized in order to reduce attenuation and maximize the diffraction signal-to-noise ratio. Consequently we designed and built a separator-free sample environment for *operando* characterization, whereby two electrodes (NMC *vs* Li metal in this work) can be sufficiently isolated opposite one another for electrochemical operation and characterization without the need for a separating material such as glass fiber (see Figure 6). This setup allowed the authors to tailor the separation of the two electrodes so that the electrochemical performance could be optimized while also allowing both the incident and diffracted beams to undergo minimal unnecessary attenuation, thus maximizing the detector signal. The stability of the cell current during acquisition also confirms that insignificant amounts of free radicals were produced during open beam (see the Supporting Information).

The cell consisted of two cylindrical stainless steel electrical terminals placed end-to-end, inside a poly(ether ether ketone) (PEEK) housing and sealed with perfluoroalkoxyalkane (PFA) Swagelok unions and ferrules. The terminals are fabricated such that 1 mm stainless steel dowels can be secured inside the PEEK housing (Figure 6a). This allows established sample preparation methods such as laser micromachining[35] and focused-ion-beam (FIB) milling[24] to be applied to the material of interest before assembly, further reducing unnecessary beam attenuation.

The material of interest in this work was commercially printed NMC811 cathode sheets (NEI Corp., USA). Scanning electron microscope (SEM) images can be found within the Supporting Information (Figure S1). The cathode sheet consisted of 90% active material, 5% poly(vinylidene fluoride) binder, and 5% carbon black coated onto an aluminum current collector. The primary particles for these materials have features of around 0.75 μm, with a variety of secondary particle sizes in order to optimize packing density: 3−30 μm (d_{50}, 10−13 μm) with an areal loading of 2 mAh cm^{-2} ± 5%, and a purity above 98%. This material is supplied as sheets that are 12.7 cm × 25.4 cm in area, with a tape thickness of 58−60 μm and a 16 μm current collector thickness.

To conduct the BCDI experiment, a 1 mm disk was punched from the sheet and secured to the top of a 1 mm stainless steel dowel using conductive epoxy (Chemtronics, Hoofddorp, Netherlands) and then machined using a laser micromachining tool (Oxford Lasers, U.K.) to a diameter of 90 μm for assembly; a full schematic and assembly procedure can be found within the Supporting Information (Figure S2). The cell was filled with LiPF$_6$ in ethylene carbonate/ethyl methyl carbonate (EC:EMC, 3:7, v/v) with 2 wt % vinylene carbonate as the electrolyte.

Bragg Coherent Diffraction Imaging. The BCDI experiment was performed at the I13-1 Beamline at the Diamond Light Source, U.K. The cell was mounted in the horizontal scattering geometry, and the incident X-ray beam was set to 11 keV and was focused using a Fresnel zone plate behind a 400 μm diameter aperture to a slightly defocused size of 2−3 μm. The diffraction from the sample was measured using an Excalibur 3 M detector (55 μm pixel size) positioned 2.9 m away from the sample which ensured oversampling of the diffraction patterns. The oversampling condition, that there are more than two detector pixels for each diffraction fringe in each direction, is necessary for the successful inversion of the diffraction pattern into real space. The sample and the detector were aligned to the NMC811 (003) Bragg peak; this was chosen because this reflection has the highest structure factor and thus is the most likely to deliver sufficient signal for reconstruction. Moreover, the (003) planes correspond to the interlayer spacings of the TM oxide layers and are highly sensitive to variations in Li$^+$ concentration within the NMC structure. The detector is placed in-plane with the Bragg angle in the horizontal plane, so that the powder ring is vertical on the detector. The selected diffraction patterns from individual crystals were scanned in θ (vertical axis, the rocking curve angle) over a 1° range around the selected Bragg peak with a step size of 0.005° to measure the full 3D intensity distribution.

To examine the pristine material, a sample was mounted *ex situ* after undergoing two diagnostic/formation cycles that were performed at C/20 with lower and upper cutoff voltages of 3.0 and 4.3 V, respectively. Crystals I and II were reconstructed from this sample. During the *operando* measurements, the cell was secured to the beamline stage using an electrically insulating mount and then charged and discharged to various voltage points at C/2. The cell voltage was held constant during the measurement of the selected diffraction patterns. To examine charging (delithiation), crystal III was imaged at 2.7 and 3.5 V (*vs* Li/Li$^+$), and to examine discharging (lithiation), crystals IV and V were imaged at 4.1, 4.0, and 3.9 V (again *vs* Li/Li$^+$). In-depth descriptions of the electrochemical histories of each respective crystal can be found within the Supporting Information along with the cell potential and current readings.

The diffraction patterns obtained were converted into real space images using phase retrieval algorithms which were performed in MATLAB R2018a using a version of the "matlabPhasing" package;[33] iterative calculations were conducted using Shrinkwrap;[36] and a guided approach[18] was used together with the Error Reduction (ER), Hybrid Input Output (HIO),[17] Relaxed Averaged Alternating Reflections (RAAR), and Difference Map (DM) algorithms.[37] Once reconstructed, the 3D images were visualized using the software ParaView version 5.6.[38]

ASSOCIATED CONTENT

Supporting Information

The Supporting Information is available free of charge at https://pubs.acs.org/doi/10.1021/acsnano.0c08575.

> Additional discussion; Figures S1−S7 including SEM images of the raw powders, full design schematics of the nanocell, electrochemical cycling data, and additional BCDI reconstructions; and Tables S1−S4 listing pattern data and COM (PDF)

AUTHOR INFORMATION

Corresponding Author

Paul R. Shearing − *Electrochemical Innovation Lab, Department of Chemical Engineering, University College London, London WC1E 7JE, United Kingdom; The Faraday Institution, Didcot, Oxon OX11 0RA, United Kingdom;* orcid.org/0000-0002-1387-9531; Email: p.shearing@ucl.ac.uk

Authors

Ana Katrina C. Estandarte − *Electrochemical Innovation Lab, Department of Chemical Engineering, University College London, London WC1E 7JE, United Kingdom*

Jiecheng Diao − *Department of Physics and Astronomy, University College London, London WC1E 6BT, United Kingdom*

Alice V. Llewellyn − *Electrochemical Innovation Lab, Department of Chemical Engineering, University College London, London WC1E 7JE, United Kingdom; The Faraday Institution, Didcot, Oxon OX11 0RA, United Kingdom*

Anmol Jnawali − *Electrochemical Innovation Lab, Department of Chemical Engineering, University College London, London WC1E 7JE, United Kingdom*

Thomas M. M. Heenan − *Electrochemical Innovation Lab, Department of Chemical Engineering, University College London, London WC1E 7JE, United Kingdom; The Faraday Institution, Didcot, Oxon OX11 0RA, United Kingdom;* orcid.org/0000-0001-9912-4772

Sohrab R. Daemi − *Electrochemical Innovation Lab, Department of Chemical Engineering, University College London, London WC1E 7JE, United Kingdom*

Josh J. Bailey − *Electrochemical Innovation Lab, Department of Chemical Engineering, University College London, London*

WC1E 7JE, United Kingdom
Silvia Cipiccia − *Diamond Light Source, Didcot, Oxon OX11 0DE, United Kingdom*
Darren Batey − *Diamond Light Source, Didcot, Oxon OX11 0DE, United Kingdom*
Xiaowen Shi − *Diamond Light Source, Didcot, Oxon OX11 0DE, United Kingdom*
Christoph Rau − *Diamond Light Source, Didcot, Oxon OX11 0DE, United Kingdom*
Dan J. L. Brett − *Electrochemical Innovation Lab, Department of Chemical Engineering, University College London, London WC1E 7JE, United Kingdom; The Faraday Institution, Didcot, Oxon OX11 0RA, United Kingdom;* orcid.org/0000-0002-8545-3126
Rhodri Jervis − *Electrochemical Innovation Lab, Department of Chemical Engineering, University College London, London WC1E 7JE, United Kingdom; The Faraday Institution, Didcot, Oxon OX11 0RA, United Kingdom*
Ian K. Robinson − *Department of Physics and Astronomy, University College London, London WC1E 6BT, United Kingdom; The Faraday Institution, Didcot, Oxon OX11 0RA, United Kingdom; Brookhaven National Laboratory, Upton, New York 11973-5000, United States*

Complete contact information is available at:
https://pubs.acs.org/10.1021/acsnano.0c08575

Author Contributions

The manuscript was written through contributions of all authors. All authors have given approval to the final version of the manuscript. Conceptualization: A.K.C.E., R.J., I.K.R., and P.R.S. Methodology: A.K.C.E., T.M.M.H., A.V.L., S.R.D., R.J., I.K.R., and P.R.S. Preparation: A.K.C.E., T.M.M.H., A.V.L., and S.R.D. Investigation: All authors. Analysis: A.K.C.E., J.D., and T.M.M.H. Writing: All authors. Supervision, directing, and funding acquisition: R.J., D.B., I.K.R., and P.R.S.

Notes

The authors declare no competing financial interest.

ACKNOWLEDGMENTS

This work was supported by an EPSRC Grant EP/I022562/1, “Phase modulation technology for X-ray imaging”, and funding from Faraday Institution, Grants EP/S003053/1 FIRG001 and FIRG013. We also acknowledge the Royal Academy of Engineering (Grant CiET1718\59) for financial support. Work at Brookhaven National Laboratory was supported by the U.S. Department of Energy, Office of Science, Office of Basic Energy Sciences, under Contract No. DE-SC0012704. Experiments were carried out at The Diamond Lightsource, beamline I13-1 under experiments MG25852, MG25440, MG24129, MG22373, MG22309, and MG21652.

REFERENCES

(1) Xu, J.; Lin, F.; Doeff, M. M.; Tong, W. A Review of Ni-Based Layered Oxides for Rechargeable Li-Ion Batteries. *J. Mater. Chem. A* **2017**, *5*, 874−901.

(2) Liu, W.; Oh, P.; Liu, X.; Lee, M.; Cho, W.; Chae, S.; Kim, Y.; Cho, J. Nickel-Rich Layered Lithium Transition-Metal Oxide for High-Energy Lithium-Ion Batteries. *Angew. Chem., Int. Ed.* **2015**, *54*, 4440−4457.

(3) Mizushima, K.; Jones, P. C.; Wiseman, P. J.; Goodenough, J. B. Li_xCoO_2 (0< X←1): A New Cathode Material for Batteries of High Energy Density. *Mater. Res. Bull.* **1980**, *15*, 783−789.

(4) Min, K.; Kim, K.; Jung, C.; Seo, S.-W.; Song, Y. Y.; Lee, H. S.; Shin, J.; Cho, E. A Comparative Study of Structural Changes in Lithium Nickel Cobalt Manganese Oxide as a Function of Ni Content during Delithiation Process. *J. Power Sources* **2016**, *315*, 111−119.

(5) Bak, S. M.; Hu, E.; Zhou, Y.; Yu, X.; Senanayake, S. D.; Cho, S. J.; Kim, K. B.; Chung, K. Y.; Yang, X. Q.; Nam, K. W. Structural Changes And Thermal Stability Of Charged $LiNi_xMn_yCo_zO_2$ Cathode Materials Studied By Combined *in Situ* Time-Resolved XRD and Mass Spectroscopy. *ACS Appl. Mater. Interfaces* **2014**, *6*, 22594−22601.

(6) Dixit, M.; Markovsky, B.; Schipper, F.; Aurbach, D.; Major, D. T. Origin of Structural Degradation during Cycling and Low Thermal Stability Of Ni-Rich Layered Transition Metal-Based Electrode Materials. *J. Phys. Chem. C* **2017**, *121*, 22628−22636.

(7) Gilbert, J. A.; Shkrob, I. A.; Abraham, D. P. Transition Metal Dissolution, Ion Migration, Electrocatalytic Reduction and Capacity Loss in Lithium-Ion Full Cells. *J. Electrochem. Soc.* **2017**, *164*, A389−A399.

(8) Konishi, H.; Yoshikawa, M.; Hirano, T. The Effect of Thermal Stability for High-Ni-Content Layer-Structured Cathode Materials, $LiNi_{0.8}Mn_{0.1-X}Co_{0.1}Mo_xO_2$ (X= 0, 0.02, 0.04). *J. Power Sources* **2013**, *244*, 23−28.

(9) Xiong, D. J.; Ellis, L. D.; Li, J.; Li, H.; Hynes, T.; Allen, J. P.; Xia, J.; Hall, D. S.; Hill, I. G.; Dahn, J. R. Measuring Oxygen Release from Delithiated $LiNi_xMn_yCo_{1-X-Y}O_2$ and its Effects on the Performance of High Voltage Li-Ion Cells. *J. Electrochem. Soc.* **2017**, *164*, A3025−A3037.

(10) Xu, Z.; Jiang, Z.; Kuai, C.; Xu, R.; Qin, C.; Zhang, Y.; Rahman, M. M.; Wei, C.; Nordlund, D.; Sun, C. J.; Xiao, X.; et al. Charge Distribution Guided by Grain Crystallographic Orientations in Polycrystalline Battery Materials. *Nat. Commun.* **2020**, *11* (1), 83.

(11) Daemi, S. R.; Lu, X.; Sykes, D.; Behnsen, J.; Tan, C.; Palacios-Padros, A.; Cookson, J.; Petrucco, E.; Withers, P. J.; Brett, D. J. L.; Shearing, P. R. 4D Visualisation of *in Situ* Nano-Compression of Li-Ion Cathode Materials to Mimic Early Stage Calendering. *Mater. Horiz.* **2019**, *6*, 612−617.

(12) Heenan, T. M. M.; Tan, C.; Hack, J.; Brett, D. J. L.; Shearing, P. R. Developments in X-Ray Tomography Characterization for Electrochemical Devices. *Mater. Today* **2019**, *31*, 69−85.

(13) Heenan, T. M. M.; Finegan, D. P.; Tjaden, B.; Lu, X.; Iacoviello, F.; Millichamp, J.; Brett, D. J.; Shearing, P. R. 4D Nano-Tomography of Electrochemical Energy Devices Using Lab-Based X-Ray Imaging. *Nano Energy* **2018**, *47*, 556−565.

(14) Xie, Z.-H.; Jiang, Z.; Zhang, X. Promises and Challenges of *in Situ* Transmission Electron Microscopy Electrochemical Techniques in the Studies of Lithium Ion Batteries. *J. Electrochem. Soc.* **2017**, *164*, A2110.

(15) Robinson, I.; Harder, R. Coherent X-Ray Diffraction Imaging of Strain at the Nanoscale. *Nat. Mater.* **2009**, *8*, 291−298.

(16) Williams, G. J.; Pfeifer, M. A.; Vartanyants, I. A.; Robinson, I. K. Three-Dimensional Imaging of Microstructure in Au Nanocrystals. *Phys. Rev. Lett.* **2003**, *90*, 175501.

(17) Fienup, J. R. Phase Retrieval Algorithms: A Comparison. *Appl. Opt.* **1982**, *21*, 2758−2769.

(18) Chen, C.-C.; Miao, J.; Wang, C. W.; Lee, T. K. Application Of Optimization Technique to Noncrystalline X-Ray Diffraction Microscopy: Guided Hybrid Input-Output Method. *Phys. Rev. B: Condens. Matter Mater. Phys.* **2007**, *76*, 064113.

(19) Ulvestad, A.; Singer, A.; Clark, J. N.; Cho, H. M.; Kim, J. W.; Harder, R.; Maser, J.; Meng, Y. S.; Shpyrko, O. G. Topological Defect Dynamics In *Operando* Battery Nanoparticles. *Science* **2015**, *348*, 1344−1347.

(20) Singer, A.; Zhang, M.; Hy, S.; Cela, D.; Fang, C.; Wynn, T. A.; Qiu, B.; Xia, Y.; Liu, Z.; Ulvestad, A.; Hua, N.; et al. Nucleation of Dislocations and Their Dynamics in Layered Oxide Cathode Materials during Battery Charging. *Nat. Energy* **2018**, *3*, 641−647.

(21) Tan, C.; Daemi, S. R.; Taiwo, O. O.; Heenan, T. M.; Brett, D. J.; Shearing, P. R. Evolution of Electrochemical Cell Designs for *in*

Situ and *Operando* 3D Characterization. *Materials* **2018**, *11* (11), 2157.

(22) Jung, R.; Morasch, R.; Karayaylali, P.; Phillips, K.; Maglia, F.; Stinner, C.; Shao-Horn, Y.; Gasteiger, H. A. Effect of Ambient Storage on the Degradation of Ni-Rich Positive Electrode Materials (NMC811) For Li-Ion Batteries. *J. Electrochem. Soc.* **2018**, *165* (2), A132−A141.

(23) Yan, P.; Zheng, J.; Gu, M.; Xiao, J.; Zhang, J. G.; Wang, C. M. Intragranular Cracking as a Critical Barrier for High-Voltage Usage of Layer-Structured Cathode for Lithium-Ion Batteries. *Nat. Commun.* **2017**, *8*, 14101.

(24) Chen-Wiegart, Y. K.; Liu, Z.; Faber, K. T.; Barnett, S. A.; Wang, J. 3D Analysis of a $LiCoO_2$-$Li(Ni_{1/3}Mn_{1/3}Co_{1/3})O_2$ Li-Ion Battery Positive Electrode Using X-Ray Nano-Tomography. *Electrochem. Commun.* **2013**, *28*, 127−130.

(25) Schipper, F.; Erickson, E. M.; Erk, C.; Shin, J.-Y.; Chesneau, F. F.; Aurbach, D. Recent Advances and Remaining Challenges for Lithium Ion Battery Cathodes I. Nickel-Rich, $LiNi_xCo_yMn_zO_2$. *J. Electrochem. Soc.* **2017**, *164*, A6220−A6228.

(26) Romano Brandt, L.; Marie, J. J.; Moxham, T.; Förstermann, D. P.; Salvati, E.; Besnard, C.; Papadaki, C.; Wang, Z.; Bruce, P. G.; Korsunsky, A. M. Synchrotron X-Ray Quantitative Evaluation of Transient Deformation and Damage Phenomena in a Single Nickel-Rich Cathode Particle. *Energy Environ. Sci.* **2020**, *13* (10), 3556−3566.

(27) Heenan, T. M.; Wade, A.; Tan, C.; Parker, J. E.; Matras, D.; Leach, A. S.; Robinson, J. B.; Llewellyn, A.; Dimitrijevic, A.; Jervis, R.; Quinn, P. D.; Brett, D. J. L.; Shearing, P. R. Identifying The Origins Of Microstructural Defects such as Cracking within Ni-Rich NMC811 Cathode Particles for Lithium-Ion Batteries. *Adv. Energy Mater.* **2020**, 2002655.

(28) Xu, C.; Märker, K.; Lee, J.; Mahadevegowda, A.; Reeves, P. J.; Day, S. J.; Groh, M. F.; Emge, S. P.; Ducati, C.; Mehdi, B. L.; Tang, C. C.; Grey, C. P., Bulk Fatigue Induced by Surface Reconstruction in Layered Ni-Rich Cathodes for Li-Ion Batteries. *Nat. Mater.* **2020**, DOI: 10.1038/s41563-020-0767-8.

(29) Ulvestad, A.; Cho, H. M.; Harder, R.; Kim, J. W.; Dietze, S. H.; Fohtung, E.; Meng, Y. S.; Shpyrko, O. G. Nanoscale Strain Mapping in Battery Nanostructures. *Appl. Phys. Lett.* **2014**, *104*, 073108.

(30) Li, J.; Downie, L. E.; Ma, L.; Qiu, W.; Dahn, J. R. Study of the Failure Mechanisms of $LiNi_{0.8}Mn_{0.1}Co_{0.1}O_2$ Cathode Material for Lithium Ion Batteries. *J. Electrochem. Soc.* **2015**, *162* (7), A1401−A1408.

(31) Li, T.; Yuan, X. Z.; Zhang, L.; Song, D.; Shi, K.; Bock, C. Degradation Mechanisms and Mitigation Strategies of Nickel-Rich NMC-Based Lithium-Ion Batteries. *Electrochem. Energy Rev.* **2020**, 3, 43−80.

(32) MäRker, K.; Reeves, P. J.; Xu, C.; Griffith, K. J.; Grey, C. P. Evolution of Structure and Lithium Dynamics in $LiNi_{0.8}Mn_{0.1}Co_{0.1}O_2$ (NMC811) Cathodes during Electrochemical Cycling. *Chem. Mater.* **2019**, *31* (7), 2545−2554.

(33) Clark, J. N.; Ihli, J.; Schenk, A. S.; Kim, Y. Y.; Kulak, A. N.; Campbell, J. M.; Nisbet, G.; Meldrum, F. C.; Robinson, I. K. Three-Dimensional Imaging Of Dislocation Propagation During Crystal Growth And Dissolution. *Nat. Mater.* **2015**, *14*, 780−784.

(34) Hull, D.; Bacon, D. J. *Introduction to Dislocations*, 4th ed.; Butterworth-Heinemann, 2001.

(35) Bailey, J. J.; Heenan, T. M. M.; Finegan, D. P.; Lu, X.; Daemi, S. R.; Iacoviello, F.; Backeberg, N. R.; Taiwo, O. O.; Brett, D. J. L.; Atkinson, A.; Shearing, P. R. Laser-Preparation of Geometrically Optimised Samples for X-Ray Nano-CT. *J. Microsc.* **2017**, *267* (3), 384−396.

(36) Marchesini, S.; He, H.; Chapman, H. N.; Hau-Riege, S. P.; Noy, A.; Howells, M. R.; Weierstall, U.; Spence, J. C. H. X-Ray Image Reconstruction from a Diffraction Pattern Alone. *Phys. Rev. B: Condens. Matter Mater. Phys.* **2003**, *68*, 140101.

(37) Thibault, P.; Dierolf, M.; Menzel, A.; Bunk, O.; David, C.; Pfeiffer, F. High-Resolution Scanning X-Ray Diffraction Microscopy. *Science* **2008**, *321* (80), 379−382.

(38) Ahrens, J.; Geveci, B.; Law, C. ParaView: An End-User Tool for Large Data Visualization. *Visualization Handbook*; Elsevier, 2005; pp 717−731, DOI: 10.1016/B978-012387582-2/50038-1.